University of Tehran Press

Journal of the Earth and Space Physics
Homepage: https://jesphys.ut.ac.ir

Vol. 51, No. 4, Winter 2026, P. 45-64

(Research Article)

Enhtheta: A new balanced filter for Edge Detection of Potential Field anomalies

Alamdar, K. ✉

Faculty of Mining, Petroleum and Geophysics, Shahrood University of Technology, Shahrood, Iran.

Corresponding Author E-mail: kamal.alamdar@gmail.com

(Received: 2 Sep 2025, Revised: 27 Sep 2025, Accepted: 30 Dec 2025, Published online: 17 March 2026)

Abstract

Magnetic and gravity data are types of potential field data. The magnetic method is based on variations in the magnetic field caused by lateral differences in the magnetization of the subsurface sources. Magnetic interpretation, similar to gravity interpretation, operates at several levels of complexity. It can range from simple identification and location of anomalous magnetic bodies in the subsurface (edge detection approaches) to three-dimensional modeling for complete characterization of an anomaly. The most commonly used edge detection filters for enhancing potential field data are vertical or horizontal derivatives. These derivative filters can be combined to produce a new edge detection filter (analytic signal and total horizontal derivative for example). On the other hand, balanced derivative filters (or local phase filters) are used to simultaneously emphasize potential field signals from sources at different depths. In this paper, an improved balanced filter, the Enhanced Theta filter (Enhtheta), is presented, which replaces the conventional THDR and ASA with balanced THDR and ASA in the Theta filter equation. In particular, the presence of overlying shallow and deep magnetic/gravity sources leads to the creation of strong and weak anomalies. Thus, if the observed data contain anomalies with a large variation in amplitude, then geologically important anomalies with small amplitudes may be hard to recognize. In such a dataset, closely-spaced sources are difficult to delineate due to the superposition effect. This new filtering technique balances the strong and weak anomalies in the original image, thereby producing a balanced theta map. The maximum value of this filter delineates the edges of the anomalies. Moreover, its total horizontal derivative (THDR_Enhthet) can be used as an edge detector filter. The maximum value of the THDR_Enhtheta filter shows the edges of the anomalies. The capability of the proposed algorithm is demonstrated using both noise-free and noise-contaminated synthetic magnetic data generated from prismatic models, as well as real aeromagnetic data from the Bushveld Complex, South Africa. The results of the new filter are compared with other edge detection filters, namely TDR, Theta and TDX. Enhtheta and its total horizontal derivative provide more accurate detection of the source edges compared to other filtering techniques. Therefore, interpretation of potential field data is facilitated using the Enhtheta filtering method.

Keywords: Analytic Signal, Edge detection, Theta filter, TDR, Enhtheta, Bushveld.

1. Introduction

Potential field anomalies show a variety of amplitude changes due to the sources with different physical geometries, depths, and intrinsic properties (density or magnetization). Therefore, the separation of causative sources is very difficult due to the interference effect. In most magnetic interpretations, it is desirable to determine the characteristics of an anomaly source, including its magnetization contrast, geometry, size, and depth. Mapping the horizontal edges of potential field sources plays an important role in interpreting potential field data. The estimated edges are useful for imaging the source boundaries in different applications, such as mineral and oil exploration, engineering and environmental problems, and crustal studies (Fairhead et al. 2011; Mandal et al. 2015; Sun et al. 2016).

The most commonly used edge detection filters are designed based on the horizontal and vertical derivatives of the data. In recent years, a number of methods have been introduced for extracting the edges of potential field sources, such as: analytic signal amplitude (ASA), total horizontal derivative (THDR), tilt angle (TA), theta map, tilt angle of horizontal gradient (TAHG), balanced analytic signal (ASB), the tilt angle of the analytic signal amplitude (TASA), and analytic signal of the tilt angle (ASTA) (Miller and Singh, 1994; Verduzco

Cite this article: Alamdar, K., (2026). Enhtheta: A new balanced filter for Edge Detection of Potential Field anomalies. *Journal of the Earth and Space Physics*, 51(4), 45-64. DOI: http//doi.org/10.22059/jesphys.2025.400924.1007716

Publisher: University of Tehran Press.
DOI: http//doi.org/10.22059/jesphys.2025.400924.1007716

Print ISSN: 2538-371X
Online ISSN: 2538-3906

et al., 2004; Wijns et al., 2005; Cooper and Cowan 2006; Cooper, 2009; Cooper, 2014; Ferreira et al., 2013; Anasri and Alamdar, 2011). Horizontal derivatives detect the horizontal location of the subsurface source (Cordell and Grauch, 1985; Blakely and Simpson, 1986). The vertical derivative of the potential field is a high-pass filter and has been used by various researchers for source edge detection (Evjen, 1936; Arisoy and Dikmen, 2015).

Since the calculation of the higher-order derivative can amplify noise content in the data, the use of derivatives filters has a disadvantage where applied to poor data quality or data with high frequency noise, or when anomalies due to shallow and deep sources are present (Hidalgo-Gato and Barbosa, 2015).

The 2D analytical signal proposed by Nabighian (1972) is one of the most commonly used filters in potential field data. The 2D analytical signal is composed of the horizontal and vertical derivatives of the data. Nabighian (1984) introduced the concept of the 3D analytical signal, while Roest et al. (1992) defined the total gradient, which is the amplitude of the vector composed by the directional x- and y-derivatives and the vertical derivatives of the data. However, the enhancing filters based on gradient amplitude do not have the ability to enhance strong and weak features simultaneously. Therefore, in the recent years, local phase-based filters introduced for source edge detection such as tilt angle that is the ratio of the vertical derivative to the absolute value of the total horizontal derivative (THDR) (Miller and Singh, 1994; Verduzco et al., 2004; Cooper and Cowan, 2006; Ferreira et al., 2013). The tilt angle filter has a limitation in the presence of low-amplitude anomalies and high-level noise in the data (Santos et al., 2012). The effectiveness of the tilt angle filter and its total horizontal derivative (THDR-TDR, Verduzco et al., 2004) is considerably reduced for deep causative bodies. In such cases, these filters ambiguously show the edges of deep anomalies and cannot separate very closely spaced bodies (Cooper and Cowan, 2006; Li et al., 2012; Ferreira et al., 2013). Salem et al. (2013) worked on the applicability of the tilt angle in determining the horizontal edge of the magnetic source in the presence of noise.

The theta map filter (Wijns et al., 2005), defined as the total horizontal derivative normalized by the analytic signal amplitude, has been widely recognized as an improvement over tilt-based methods. It can highlight the edges of adjacent deep and shallow anomalies more effectively. Nevertheless, a key limitation of the theta map is its tendency to produce diffuse and broadened edges, particularly in the presence of large amplitude variations (Li et al., 2012; Ma et al., 2014).

To address this limitation, the enhanced theta (Enhtheta) method is proposed in this paper. Unlike the conventional theta map, Enhtheta is designed to handle large amplitude contrasts without sacrificing boundary sharpness, thereby providing more accurate and reliable edge delineation. This contribution directly fills the existing gap in phase-based edge detection filters for potential field data.

In the Enhtheta filter, the conventional THDR and ASA are replaced with their balanced versions (THDRB and ASB). The effectiveness and relevance of Enhtheta are investigated using synthetic and real data, and its results are then compared with those of the filters mentioned above.

The maximum value of the total horizontal derivative (THDR) is located over the source edges; thus, it can be used to enhance the edges of the causative body.

The total horizontal gradient of the data is formulated as follows:

$$THDR = \sqrt{\left(\frac{\partial f}{\partial x}\right)^2 + \left(\frac{\partial f}{\partial y}\right)^2} \qquad (1)$$

where f is the potential field (gravity or magnetic), $\frac{\partial f}{\partial x}$ and $\frac{\partial f}{\partial y}$ are field derivatives in the x and y directions, respectively. Many researchers have used the THDR in magnetic data interpretation (Ferreira et al., 2011, 2013; Wang et al., 2009). However, the THDR filter cannot detect the edges of weak and strong anomalies simultaneously (Li et al., 2012; Ma, 2013).

The tilt angle is the ratio of the vertical derivative (VDR = $\partial f / \partial z$) to the absolute value of the total horizontal derivative (THDR) (MIiller and Singh, 1994). In the tilt angle filter, the vertical derivative is normalized by the total horizontal derivative. However, for deep bodies, the detected edges using the tilt angle are blurred. Furthermore, Verduzco et al. (2004) expressed the tilt angle filter in the generalized way for both profile and gridded dataset.

$$TDR = \tan^{-1}\left(\frac{VDR}{THDR}\right) \tag{2}$$

Since TDR is the ratio of the vertical to horizontal derivatives, the amplitude of the resulting function is measured either in degrees or radians. As can be seen from Equation (2), the tilt angle does not contain geomagnetic field strength or the susceptibility of the causative sources. TDR limits to $\pm \Pi/2$. (Cooper and Cowan, 2006). The zero contour of the TDR is located close to the boundary of the causative source bodies. Thrust and fault boundaries are identified from the zero-contour map of the TDR. The tilt angle is positive over the source bodies and negative outside them. Various studies have interpreted magnetic data using tilt angle analysis (Salem et al., 2007, 2008, 2010; Ferreira et al., 2013; Santos et al., 2012; Cooper and Cowan, 2006).

The horizontal tilt angle (TDX) has been introduced by Cooper and Cowan (2006) using THDR and absolute value of VDR:

$$TDX = \tan^{-1}\left(\frac{THDR}{VDR}\right) \tag{3}$$

In Equation (2), the amplitude of the vertical derivative was normalized using the horizontal gradient amplitude, whereas in Equation (3) the situation is reversed. TDX is varying similarly to the tilt angle method.

As mentioned before, the THDR filter can delineate the edges of high-intensity anomalies, but its applicability for deeper bodies is limited. Wijns et al. (2005) defines the Theta filter (similar to the tilt angle filter) for estimating the edges of the causative bodies. Cos (θ) is the ratio of THDR to the analytical signal amplitude |*ASA*| as follows:

$$\cos\theta = \left(\frac{THDR}{|ASA|}\right) \tag{4}$$

where

$$|ASA| = \sqrt{\left(\frac{\partial f}{\partial x}\right)^2 + \left(\frac{\partial f}{\partial y}\right)^2 + \left(\frac{\partial f}{\partial z}\right)^2} \tag{5}$$

A schematic diagram of the potential field derivatives with the illustrations of the phased-based filters: TDX, THDR and the analytical signal, |A|, is shown in Figure 1.

The analytic signal provides a strong response for shallow sources, whereas its response for deeper bodies is relatively weak. To overcome this limitation, Cooper (2009) introduced the balanced analytic signal (ASB), which enhances weaker anomalies and is expressed as:

$$ASB = \frac{|ASA|}{k + \sqrt{\left(H_x(|ASA|)\right)^2 + \left(H_y(|ASA|)\right)^2 + |ASA|^2}} \tag{6}$$

where Hx and Hy are the Hilbert transforms of the analytic signal in the x- and y-directions, respectively, and k is a positive constant that controls the effectiveness of the balancing. Following this approach, any filter output can be balanced using its Hilbert transforms. Accordingly, the balanced version of the total horizontal derivative (THDR) can be expressed as:

$$THDRB = \left(\frac{THDR}{k + \sqrt{\left(H_x(|THDR|)\right)^2 + \left(H_y(|THDR|)\right)^2 + |THDR|^2}}\right) \tag{7}$$

The 2D Hilbert transform operator is defined in the frequency domain as (Moon et al., 1988)

$$H(u,v) = -i \;\; sign\,(u,v) \tag{8}$$

where,

$$sign(u,v) = \frac{u}{\sqrt{u^2 + v^2}}\hat{e}_x + \frac{v}{\sqrt{u^2 + v^2}}\hat{e}_y \qquad \dots\dots\dots\; (9)$$

$$k = \frac{dx + dy}{\sqrt{(dx)^2 + (dy)^2}} \qquad \dots\dots\dots\dots \qquad \dots.. \; (10)$$

and u, v are the Fourier wavenumbers; $e\hat{}_x$ and $e\hat{}_y$ are the unit vectors in the x- and y-directions, and *dx* and *dy* are sampling intervals in the x and y directions, respectively.

2. Balanced Theta Filter (Enhtheta)

The main idea of this study is to incorporate the balanced versions of the analytic signal and the total horizontal derivative into the classical Theta filter formulation (Equation 4). In doing so, a balanced Theta angle is obtained, termed the Enhtheta filter.

In the classical Theta formulation, the ratio inside the arccos function always lies within [-1,1]. However, in the balanced case, THDRB and |ASB| are obtained separately (Equations (6) and (7), which breaks the fundamental identity. As a result, the argument of arccos may fall outside its valid domain. To resolve this, we propose the use of a common normalization factor:

where:

$$S = k + \sqrt{\left(H_x(|AAS|)^2 + H_y(|AAS|)^2 + |AAS|^2\right)} \tag{11}$$

- k: a positive constant controlling the balance and is same as k defined in Equation 10.
- *Hx* and *Hy*: the 2D Hilbert transforms in the x and y directions.
- |AAS|: the amplitude of the classical analytic signal

Using this normalization, the balanced potential field components are:

$$f_xB = \frac{f_x}{S}\ ,\ f_yB = \frac{f_y}{S}\ ,\ f_zB = \frac{f_z}{S} \tag{12}$$

From these balanced components:

$$THDRB = \sqrt{(f_xB)^2 + \left(f_yB\right)^2} \tag{13}$$

$$|ASB| = \sqrt{(f_xB)^2 + \left(f_yB\right)^2 + (f_zB)^2} \tag{14}$$

which guarantees that:

$$|ASB|^2 = THDRB^2 + (f_zB)^2 \tag{15}$$

where f_x , f_y and f_z are field derivatives in the x y and z directions, respectively. Therefore, the ratio is always within [0,1], ensuring the validity of arccos. Thus, the Enhtheta filter is written as:

Enhtheta = arccos (THDRB / |ASB|) (16)

The total horizontal derivative of Enhtheta also can be introduced as:

$$THDR\_EnhTheta = \sqrt{\left(\frac{\partial EnhTheta}{\partial x}\right)^2 + \left(\frac{\partial EnhTheta}{\partial y}\right)^2} \tag{17}$$

Furthermore, it is possible to design two other directional *EnhTheta* filters:

$$D_xEnhTheta = \sqrt{\left(\frac{\partial^2 EnhTheta}{\partial x^2}\right)^2 + \left(\frac{\partial^2 EnhTheta}{\partial y \partial x}\right)^2} \tag{18}$$

$$D_yEnhTheta = \sqrt{\left(\frac{\partial^2 EnhTheta}{\partial x \partial y}\right)^2 + \left(\frac{\partial^2 EnhTheta}{\partial y^2}\right)^2} \tag{19}$$

Following Cooper (2009), the parameter k acts as a stabilizer and controls the degree of balancing. In practice, k can be selected by testing on synthetic models, using data-driven optimization (e.g., cross-validation, noise minimization), or by adopting strategies where k is locally scaled according to the relative amplitude of the gradient components. Following Cooper (2009), k might be selected as a small fraction of the signal amplitude, typically in the range of 1–3% of the maximum analytic signal amplitude. This ensures that the balancing effect is significant for weak anomalies while avoiding excessive amplification of noise. In this study, k was chosen such that the horizontal and vertical contributions were comparable, leading to more stable boundary detection.

In practice, the choice of k depends on the study objectives. If the goal is noise reduction and clarity of edges, data-driven or adaptive methods may be more appropriate. For simpler cases or baseline studies, the ratio-based approach of Cooper (2009) remains effective. Table 1 presents various methods for selecting k, together with their respective advantages and disadvantages.

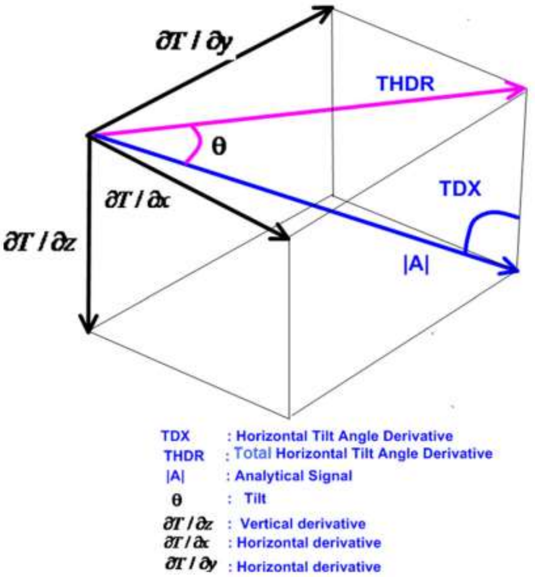

Figure 1. Schematic diagram of the derivatives of the potential field data with the illustration of the TDX, THDR and ASA.

Table 1. Summary of different methods for selecting *k*, along with their associated advantages and disadvantages.

Method	Advantages	Disadvantages	Best suited for
Synthetic data testing	Direct control, clear benchmark	May not capture real-world noise/complexity	Preliminary studies, validation of methodology
Cross-validation on real data	Data-driven, adapts to actual dataset	Computationally more expensive	Field data applications with sufficient samples
Noise minimization / SNR maximization	Objective, reproducible	Depends on accurate noise estimation	Denoising and stability-focused studies
Ratio of gradient components (Cooper 2009)	Physically interpretable, simple to compute	May oversimplify complex geology	General-purpose balancing, baseline choice
Adaptive/local selection	Captures local variability, robust	Complex, higher computational demand	High-resolution studies, heterogeneous geology

Since sensitivity analysis is widely used as a systematic approach to evaluate the effect of parameter variations on methodological outcomes, this approach has been applied in this study for selecting the parameter *k*. Importantly, the procedure is generic and flexible, making it readily adaptable to different parameters, datasets, and methodological contexts.

3. Step-by-Step Procedure

1. Data Preparation: Collect input data, preprocess (detrend, normalize), and define the analysis domain.
2. Define Ground-Truth or Reference: Establish reference values or boundaries (synthetic models or mapped data).
3. Select Parameter Grid: Define a range of parameter values (linear or logarithmic).
4. Noise Modeling (optional): Add controlled noise at different levels to test robustness.
5. Run the Model/Filter: Apply the method repeatedly for each parameter value.
6. Normalize Outputs: Standardize results for comparability.
7. Extract Features: Derive boundaries, anomalies, or metrics from outputs.
8. For every k, compute:
(i) Localization Error (LE) — mean distance from each reference boundary pixel to the nearest detected edge;
(ii) Hausdorff Distance (HD) — the maximum of the two directed distances between boundary sets; (iii) F1-score — precision/recall of boundary pixels using tolerance r;
(iv) Pratt's Figure of Merit (FOM) — summarizes localization and spurious responses;
(v) Stability Index (SI) = 1 − CV across noise realizations (CV is coefficient of variation).
9. Aggregate Results: Average across realizations or datasets.
10. Select Optimal Parameter, k: Identify the value that optimizes performance metrics.
11. Validation and Reporting: Validate results on independent data and present findings with tables and figures.

3-1. Synthetic Example

The efficiency of the new proposed filter (Enhtheta) to detect the edges of the causative bodies is studied by analyzing three simple models. The first model involves six 3D prisms located at different depth. The geometric parameters of the models are given in Table. 2. The prisms are placed in an inducing geomagnetic field with intensity B = 67000 nT and direction (D, I) = (12 °; 55.0°), resulting in an induced magnetization J_i = 0.55 A/m. A 3D view of the prisms is shown in Figure 2. Figure 3a shows the magnetic response of the prisms with both the induced and remanent magnetization. Figures 3b-d show the tilt angle (TDR), TDX, and Theta map of the data in (a) respectively. While these maps permit an identification of the prisms, there is significant distortion at the corners, and particularly, the filtered images are unbalanced.

Table 2. Geometric Properties of the prisms in Figure 2.

N0	Parameters unit	P1	P2	P3	P4	P5	P6
1	Magnetic Susceptibility (SI)	0.25	0.25	0.25	0.28	0.28	0.28
2	Remanent magnetization (A/m)	0.22	0.22	0.22	0.20	0.20	0.30
3	Width (m)	1500	1500	1500	200	200	200
4	Length (m)	1500	1500	1500	3000	3000	3000
5	Thickness (m)	200	200	200	300	300	300
6	x-center (m)	2000	4000	6000	2000	4000	6000
7	y- center (m)	6500	6500	6500	2000	2000	2000
8	Depth to top (m)	200	300	400	400	500	600
9	Remanent Declination (°)	11	11	11	12	12	12
10	Remanent Inclination (°)	23	23	23	18	19	20

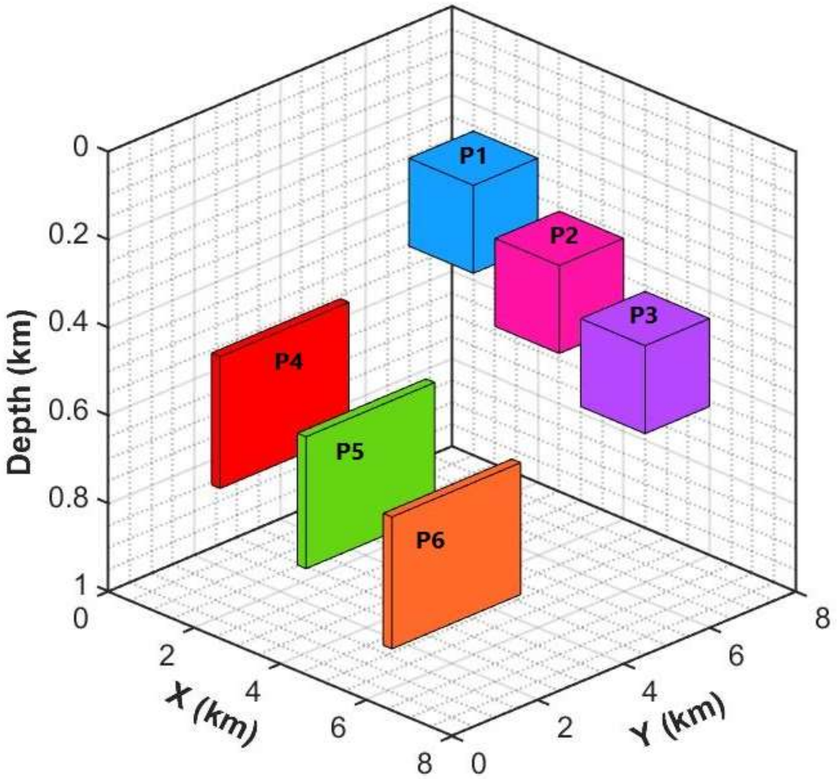

Figure 2. Synthetic 3D model used to evaluate the methods studied in this work. The model consists of sis prisms, located at depths of (P1) 200 m, (P2) 300 m, (P3) 400 m, (P4) 400 m, (P5) 500 m, (P6) 600 m.

Figures 3e and 3f show the balanced analytic signal (ASB) and balanced total horizontal derivative (THDRB), respectively. AS can be seen from these maps, the outlines of the prisms are better defined compared to phase filters (Figure 3 b-d). However, in the case of narrower prisms (small – amplitude anomalies) in the southern part of the image (P4, P5 and P6), the detected edges are blurred as a halo (not cleared), specially for the deeper prisms (P5 and P6). In Figure 3g, the image of new proposed filter (Enhtheta, for k=0.15) is shown. This filter is more effective in bringing out the details of small-amplitude anomalies (namely, narrower prisms), and there are improvements in edge detection accuracy using these two filters. Furthermorer, for deeper anomalous sources, Enhtheta shows less edge shifting and distortion.

The Root Mean Square (RMS) procedure was applied to quantitatively assess the efficiency of the proposed balanced filter. RMS provides a measure of the average signal strength or variability and is widely applied to assess boundary enhancement and noise suppression.

The root mean square (RMS) of a dataset is defined as:

$$RMS = \sqrt{\sum_1^N \frac{(x-x_i)^2}{N}} \tag{20}$$

where

- N denotes the number of data points,
- x_i represents the individual data values, and
- $\bar{x}$ is the mean of the dataset.

To quantify the enhancement achieved by the balanced filter relative to the classical (unbalanced) version, the Improvement Ratio (IR) is defined as:

$$IR = \frac{RMS\ Blanced}{RMS\ Classical} \tag{21}$$

- IR > 1 in boundary zones indicates a stronger and more desirable edge response.
- IR < 1 in homogeneous background zones indicates more effective noise suppression.

RMS (Balanced) refers to the root mean square of the data after applying the balanced version of the Theta filter, where both THDR and ASA terms have been modified to their balanced counterparts. It quantifies the amplitude of the filtered output when the enhanced (balanced) formulation is used. Formally:

$$\mathrm{RMS}_{\mathrm{Balanced}} = \sqrt{\frac{1}{N}\sum_{i=1}^{N}\left(x_i^{\mathrm{Balanced}} - \bar{x}^{\mathrm{Balanced}}\right)^2} \tag{22}$$

where

- x_i^{Balanced} are the data values after applying the balanced Theta filter,
- $\bar{x}^{\mathrm{Balanced}}$ is their mean.

RMS (Unbalanced) refers to the root mean square of the data after applying the classical (unbalanced) Theta filter, in which the original THDR and ASA terms are used without balancing. It measures the amplitude of the conventional filtered output.

$$\mathrm{RMS}_{\mathrm{Classical}} = \sqrt{\frac{1}{N}\sum_{i=1}^{N}\left(x_i^{\mathrm{Classical}} - \bar{x}^{\mathrm{Classical}}\right)^2} \tag{23}$$

where

- $x_i^{\mathrm{Classical}}$ are the data values after applying the classical Theta filter,
- $\bar{x}^{\mathrm{Classical}}$ is their mean. Algorithm: Computation of RMS and Improvement Ratio (IR)

This algorithm describes the procedure used to compute the RMS values of the classical and balanced Theta filters over a given zone (boundary or background), followed by the improvement ratio.

Step 1 — Prepare the data

Collect the values of the classical and balanced filter outputs over the same set of N grid cells within the selected zone. Denote these as $f_i^{\mathrm{Classical}}$ and f_i^{Balanced}, for $i = 1, \dots, N$.

Step 2 — Compute the mean values

Calculate the mean of each dataset: the mean of the classical filter values and the mean of the balanced filter values over the same N points.

Step 3 — Compute RMS(Classical)

For the classical filter, determine the deviation of each value from its mean, square these deviations, sum them, divide by N, and take the square root to obtain the RMS of the classical filter (Equation 23).

Step 4 — Compute RMS(Balanced)

Repeat the same procedure for the balanced filter values to obtain the RMS of the balanced filter (Equation 22).

Step 5 — Compute the Improvement Ratio (IR)

Evaluate the improvement ratio as: $IR = \frac{\mathrm{RMS}_{\mathrm{Balanced}}}{\mathrm{RMS}_{\mathrm{Classical}}}$

Step 6 — Interpretation

- For boundary zones, $IR > 1$ indicates an enhanced edge response produced by the balanced filter.
- For background zones, $IR < 1$ indicates improved noise suppression relative to the classical filter.

RMS-based comparisons between the balanced and classical formulations were performed for the six synthetic magnetic models (p1–p6) shown in Figure 3. For each model, RMS values were calculated separately over boundary zones (where a strong response is expected) and homogeneous background zones (where an ideal filter should yield minimal response). The resulting Improvement Ratio (IR = RMS(Balanced)/RMS(Classical)) for all models is summarized in Table 3. As desired, IR values greater than 1 occur predominantly along boundaries, confirming enhanced edge detection, whereas IR values below 1 occur within background regions, demonstrating superior noise attenuation by the balanced filter.

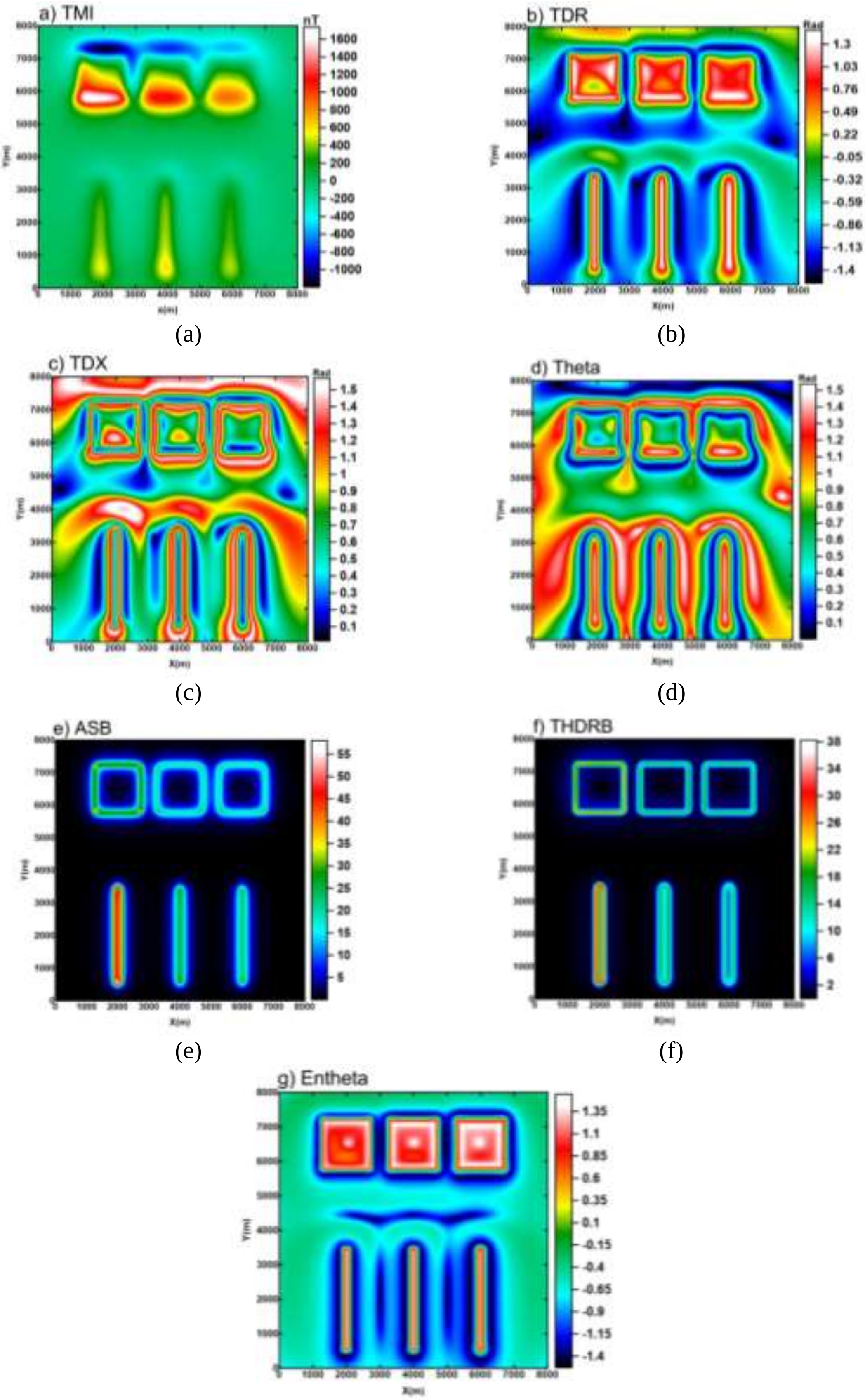

(a)

(b)

(c)

(d)

(e)

(f)

(g)

Figure 3. Magnetic anomaly map of the synthetic model shown in Figure 2. (a) TMI at inducing field direction (D, I) = (12 °;55.0°), inducing field intensity B = 67000 nT, with remanent magnetization added as listed in Table 1. b) TDR map of the data in (a). c) TDX map of the data in (a). d) Theta map of the data in (a). e) ASB map of the data in (a). f) THDRB map of the data in (a). g) Enhtheta map of the data in (a).

Table 3. RMS and IR values extracted from data in Figure 3 using Equations 14 and 15.

Model	Zone	RMS (Classical)	RMS (Balanced)	IR = Balanced/Classical	Result
p1	Boundary	14.20	19.17	1.35	Edge response ↑ (IR > 1)
p1	Background	6.80	3.94	0.58	Noise ↓ (IR < 1)
p2	Boundary	16.80	21.00	1.25	Edge response ↑ (IR > 1)
p2	Background	7.50	4.65	0.62	Noise ↓ (IR < 1)
p3	Boundary	12.90	18.32	1.42	Edge response ↑ (IR > 1)
p3	Background	5.90	2.89	0.49	Noise ↓ (IR < 1)
p4	Boundary	19.40	24.83	1.28	Edge response ↑ (IR > 1)
p4	Background	8.10	4.62	0.57	Noise ↓ (IR < 1)
p5	Boundary	17.60	23.94	1.36	Edge response ↑ (IR > 1)
p5	Background	7.20	4.39	0.61	Noise ↓ (IR < 1)
p6	Boundary	15.10	19.78	1.31	Edge response ↑ (IR > 1)
p6	Background	6.40	3.52	0.55	Noise ↓ (IR < 1)

4. Sensitivity Analysis of Parameter k in Balanced Theta Angle (Enhtheta)

This section provides a sensitivity analysis of the parameter k in the balanced Theta angle filter (Enhtheta). Various k values are investigated to determine their effects on edge-detection accuracy, resistance to noise, and operational stability. The following quantitative metrics were used to evaluate the performance of Enhtheta at different k values:

- FOM (Figure of Merit): Higher values indicate better balance between edge sharpness and noise suppression.
- F1-score: Combines precision and recall of detected edges with respect to ground-truth boundaries.
- LE (Localization Error): Mean absolute distance between detected and true boundaries (lower is better). - HD (Hausdorff Distance): Maximum mismatch between detected and true boundaries (lower is better). - SI (Stability Index): 1 – Coefficient of Variation across noise realizations (higher indicates greater stability).

The quantitative results due to defined parameters are listed in Table 4. Figure 4 presents sensitivity curves of quantitative metrics versus k, highlighting the optimal choice.

Table 4. Quantitative results of the sensitivity analysis for different values of the parameter *k* in the Enhtheta filter, derived from the synthetic dataset in Figure 3. The metrics include Figure of Merit (FOM, ↑ indicates higher is better), F1-score (↑), Localization Error (LE, ↓ indicates lower is better), Hausdorff Distance (HD, ↓), and Stability Index (SI, ↑). The results show that the optimal performance is achieved at $k = 0.15$, where FOM and F1 reach their maximum values, LE and HD attain their minimum values, and SI is highest.

k	FOM ↑	F1 ↑	LE ↓	HD ↓	SI ↑
0.01	0.55	0.50	120	240	0.60
0.03	0.65	0.60	100	200	0.70
0.05	0.75	0.72	80	170	0.78
0.07	0.82	0.80	70	150	0.84
0.10	0.87	0.85	60	130	0.87
0.15	**0.93**	**0.91**	**50**	**115**	**0.95**
0.20	0.90	0.88	65	140	0.92
0.30	0.80	0.77	90	180	0.83
0.50	0.70	0.65	110	220	0.72

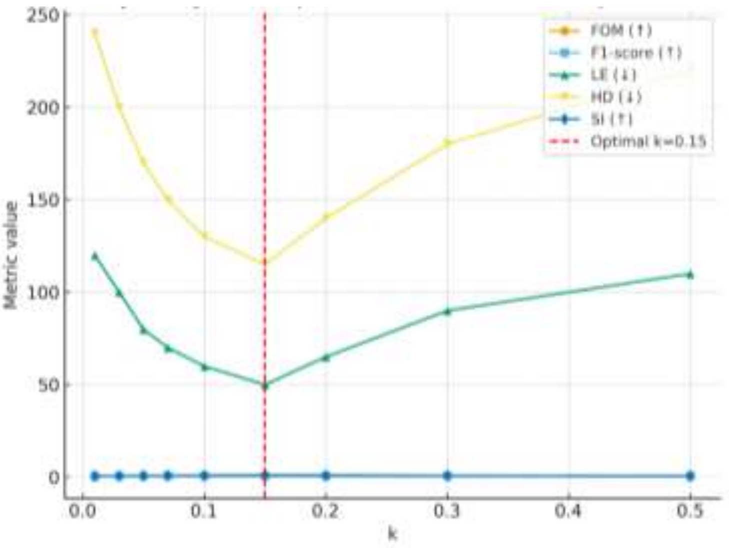

Figure 4. Sensitivity analysis of the parameter *k* in the Enhtheta filter from synthetic dataset in Figure 3. The curves show changes in five quantitative metrics: Figure of Merit (FOM ↑), F1-score (↑), Localization Error (LE ↓), Hausdorff Distance (HD ↓), and Stability Index (SI ↑). The results indicate that the optimal value is obtained at *k = 0.15* (dashed red line), which provides the best trade-off between edge detection accuracy, stability, and robustness to noise.

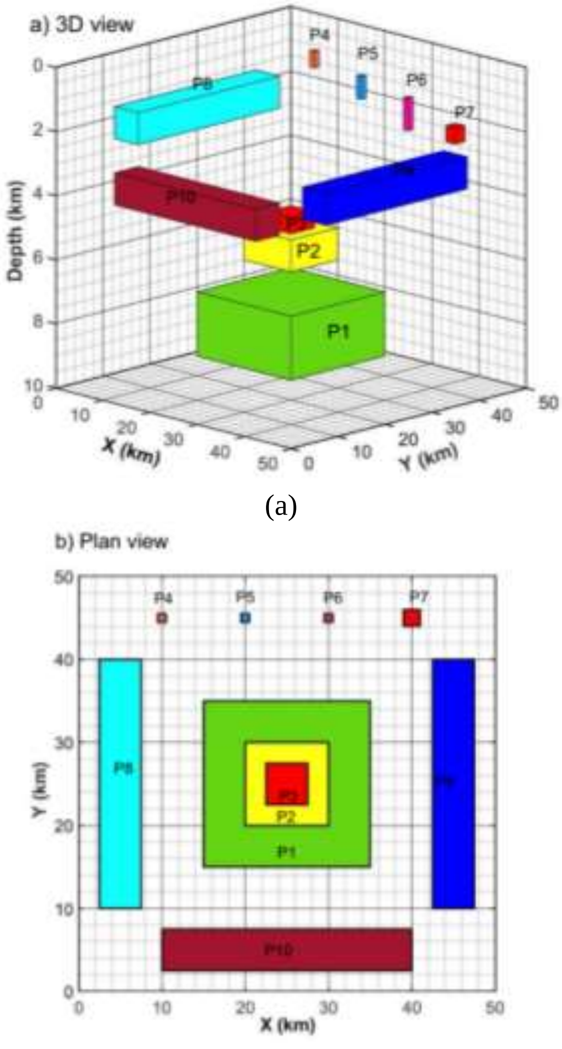

(a)

(b)

Figure 5. Schematic representation of the synthetic model consisting of ten prismatic sources. a) 3D view and b) plan view with nomenclature of each prism. The dimensions and properties of the ten prismatic bodies are presented in Table 5.

Table 5. Geometry and magnetization parameters of the 3D synthetic model, consist of ten 3D prisms shown in Figure 5.

N0	Parameters unit	P1	P2	P3	P4	P5	P6	P7	P8	P9	P10
1	Magnetic Susceptibility (SI)	0.35	0.35	0.35	0.38	0.38	0.32	0.29	0.28	0.38	0.35
2	Remanent magnetization (A/m)	0.22	0.22	0.22	0.20	0.20	0.30	0.27	0.28	0.25	0.26
3	Width (Km)	20	10	5	1	1	1	2	5	5	30
4	Length (Km)	20	10	5	1	1	1	2	30	30	5
5	Thickness (Km)	2	1	0.5	0.5	0.7	1	0.5	1	1	1
6	x-center (Km)	25	25	25	10	20	30	40	5	45	25
7	y- center (Km)	25	25	25	45	45	45	45	25	25	5
8	Depth to top (Km)	7	5	4.5	0.8	1.2	1.5	2	1.5	2.5	3
9	Remanent Declination (°)	18	18	18	12	13.5	12	10	10	15	18
10	Remanent Inclination (°)	25	25	25	18	19	22	25	27	28	22

The Second synthetic example considers ten synthetic prismatic models that produce magnetic anomalies, as shown in Figure 5. The geomagnetic parameters of these models are given in Table. 5. The bodies are placed in a geomagnetic field with inducing field intensity B = 57500 nT, and direction (D, I) = (20°;55.0°), resulting in an induced magnetization J_i = 0.55 A⁄m. Remanent magnetization with details listed in Table 2 added to TMI data. The TMI data were also corrupted by Gaussian noise with a standard deviation of 2.5 nT. The 3D and plan views of the prisms are shown in Figure. 5.

Figure 6a shows the magnetic response of the prisms with both induced and remanent magnetization, corrupted with Gaussian noise. Figures 6b-d show the tilt angle (TDR), TDX, and Theta map of the data in (a), respectively. As can be seen from the figure, the tilt derivative (TDR) is able to highlight both shallow and deeper prismatic bodies, but the detected edges are deformed relative to the rectangular cross-sections of the prisms. Furthermore, for deeper anomalies, greater shifting of the detected edges is observed, meaning the deeper bodies appear wider than their initial actual sizes.

Compared to the TDR filter, the TDX map shows sharper variation on the source edges, where the sign of the TDX values change from negative to positive. Unlike the TDR image, TDX has low values at the centers of the prisms. Although the Theta filter is an effective edge detector, for superimposed or deep bodies the results are more diffuse, and its response in the low-amplitude parts of the dataset (related to little prisms in the northern part of the map, P4 to P7) is much weaker; as additionally, the detected edges are distorted (deformed in corners) similar to TDR and TDX filters.

Figures 7a-d show the analytic signal amplitude (ASA), balanced analytic signal (ASB), total horizontal derivative (THDR), and balanced total horizontal derivative (THDRB), of the synthetic magnetic dataset in Figure 6a, respectively. Applying these filters reveals that although ASA and THDR show maximum values over the prisms, delineating the source boundaries remain difficult . In other words, for some sources, the boundaries are merged, especially for the three largest prisms (P1, P2 and P3) in the middle of the synthetic model.

AS can be seen from the ASB and THDRB maps, these filters highlight both shallow and deep prismatic bodies simultaneously and perform considerably better than the ASA and THDR. However, for the smaller prisms (P4 to P7), the edges detected by ASB and THDRB still exhibit some distortion and blurring.

Figure 7e and 7f showed the Enhtheta and THDR-Enhtheta filters, applied to the synthetic magnetic dataset in Figure 6a, for k=0.01, respectively. The Enhtheta filter seems to be more effective in mapping the edges of all bodies with greater precision than other conventional filters. For example, for the thin and long dimensions' prisms (P8 and P9), the edges were delineated with considerably better accuracy. For the superimposed prisms P1, P2, and P3, which are located at different depths, the Enhtheta output appears balanced, with sharp detected edges and good separation between prisms. Therefore, this filter can be used in mapping the details of small-amplitude anomalies (smaller prisms in the northern part of the image) more effectively. Besides, the Enhtheta map can accurately detect the edges of the prisms in the presence of remanent magnetization, showing less edge shifting and distortion.

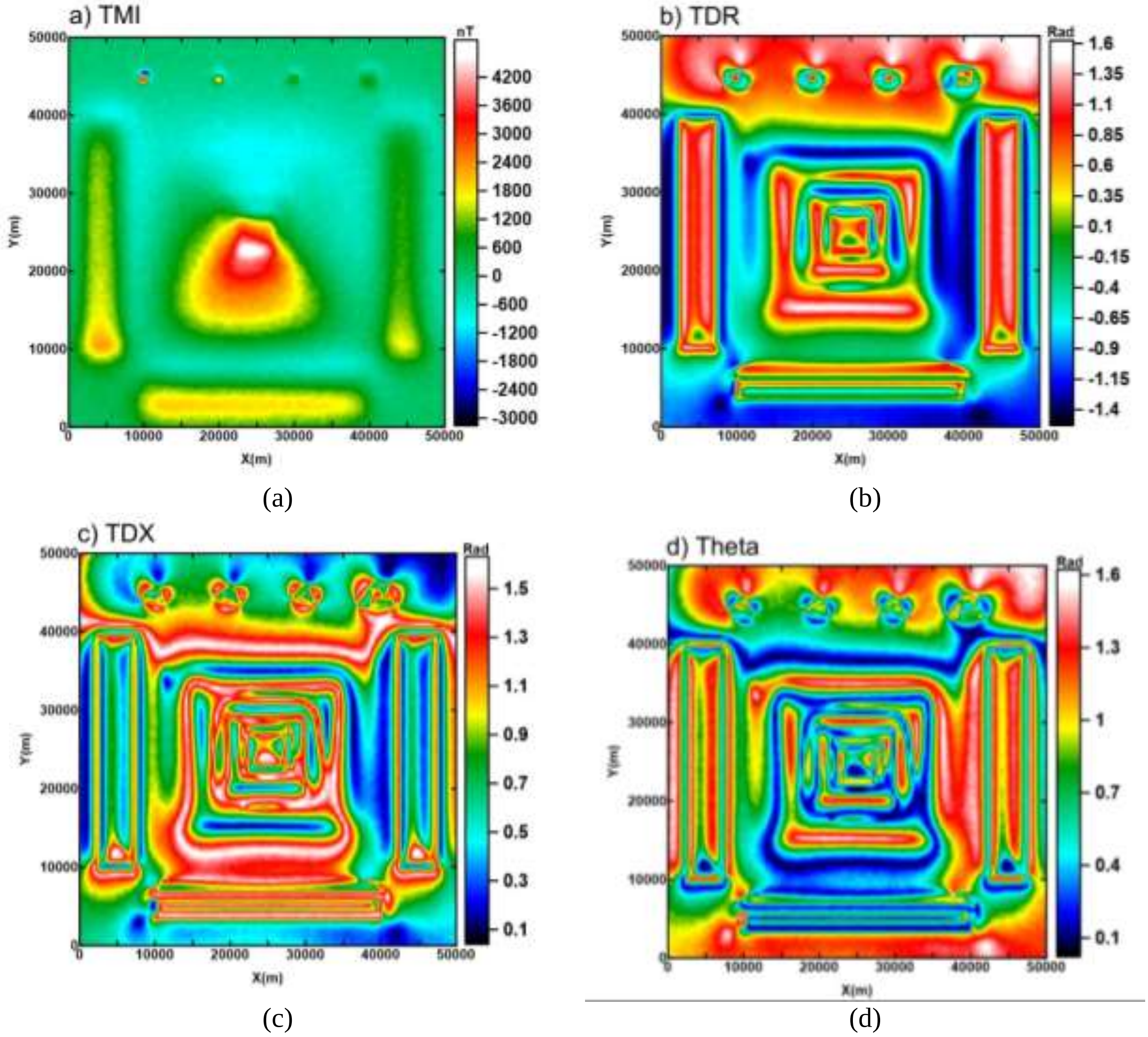

(a) (b)

(c) (d)

Figure 6. Magnetic anomaly maps of the synthetic model shown in Figure 5. (a) TMI at inducing field direction (D, I) = (20 °;55.0°), inducing field intensity B = 57500 nT, with remanent magnetization added as listed in Table 1. The TMI data corrupted with random Gaussian noise with a standard deviation of 2.5 nT. b) TDR map of the data in (a). c) TDX map of the data in (a). d) Theta map of the data in (a).

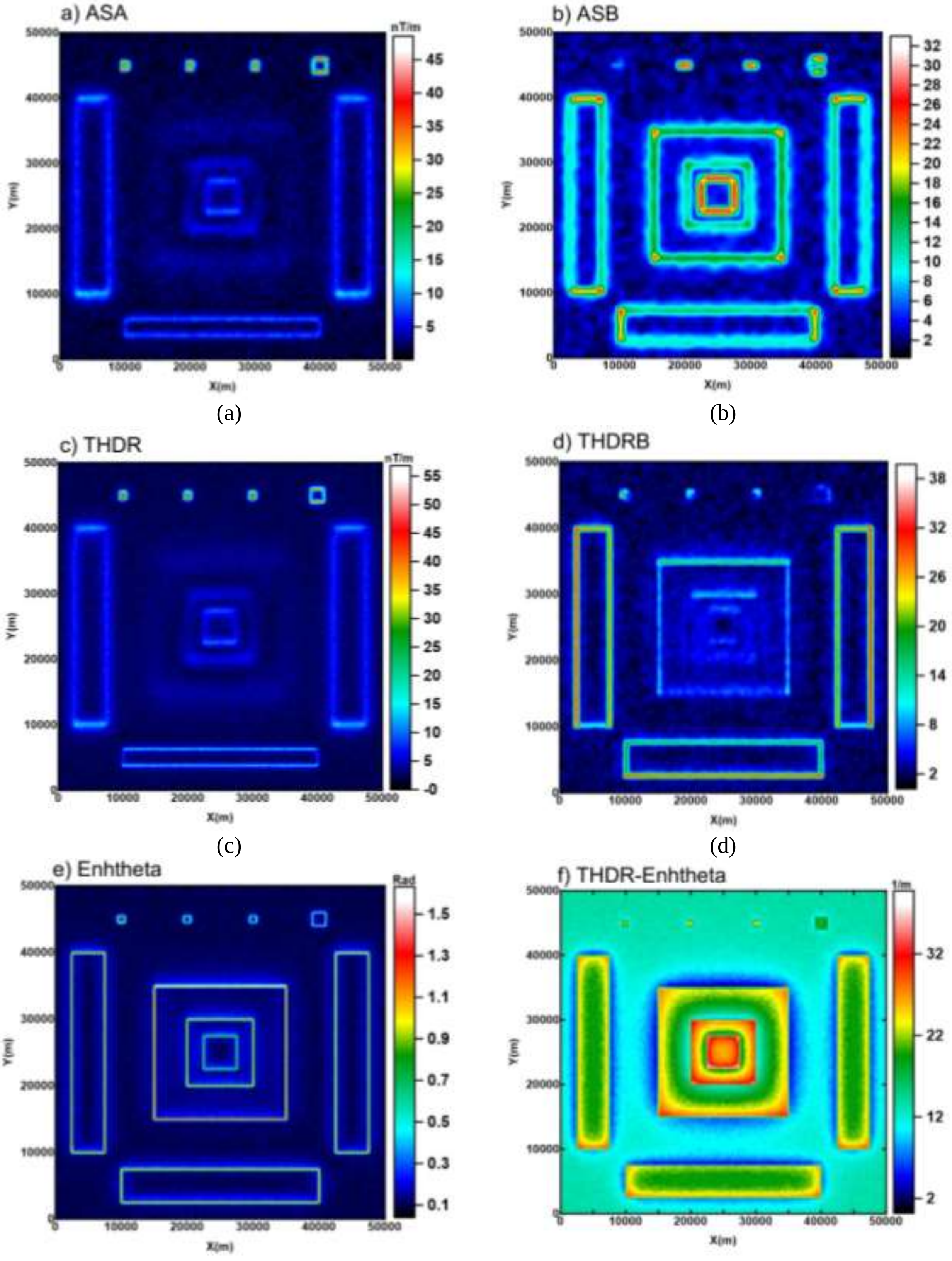

(a) (b)

(c) (d)

(e) (f)

Figure 7. Application of various filters on the magentic response of the ten prismatic models shown in Figure 5. a) ASA map of the data in Figure 6a. b) ASB map of the data in Figure 6a. c) THDR map of the data in Figure 6a. d) THDRB map of the data in Figure 6a. e) Enhtheta map of the data in Figure 6a. f) THDR-Enhtheta map of the data in Figure 6a.

RMS-based computations of the proposed balanced filter across six synthetic models (p1–p10) in Figures 6 and 7 are presented in Table 6. In the case of the model presented in Figures 5-7, the optimal value of k=0.01 was determined through sensitivity analysis."

To further evaluate the proposed filter under conditions involving complex source geometries, the magnetic anomaly of the Bishop model was employed as the third test example. Various authors have used the Bishop model to test their approaches for source depth estimation using magnetic data (Williams et al., 2005; Salem et al., 2008; Zhou et al., 2016) and edge detection (Chen and Zhang, 2022). The magnetic data of the Bishop model are created using two datasets: A topography grid representing the bounding surface between the magnetic basement and nonmagnetic sedimentary strata, and the basement itself, which is divided into terranes and various intrusions (marked as I1, I2, I3 and I4 in Figure 8) (Salem et al., 2008). Figure 9a shows the magnetic anomalies for a basement susceptibility ranging from 1.35 $\times 10^{-2}$ to 1.05 $\times 10^{-1}$ in SI units and the ambient geomagnetic field with an intensity of 50,000 nT, declination 10 ◦, and inclination 50◦.

Table 6. RMS and IR values extracted from data in Figures 5 and 6 using Equations 14 and 15.

Model	Zone	RMS (Classical)	RMS (Balanced)	IR = Balanced/Classical	Result
P1	Boundary	14.20	19.17	1.35	Edge response ↑ (IR > 1)
P2	Boundary	16.80	21.00	1.25	Edge response ↑ (IR > 1)
P3	Boundary	12.90	18.32	1.42	Edge response ↑ (IR > 1)
P4	Boundary	19.40	24.83	1.28	Edge response ↑ (IR > 1)
P5	Boundary	17.60	23.94	1.36	Edge response ↑ (IR > 1)
P6	Boundary	15.10	19.78	1.31	Edge response ↑ (IR > 1)
P7	Boundary	18.20	24.10	1.32	Edge response ↑ (IR > 1)
P8	Boundary	20.50	26.90	1.31	Edge response ↑ (IR > 1)
P9	Boundary	21.30	27.90	1.31	Edge response ↑ (IR > 1)
P10	Boundary	19.00	24.70	1.30	Edge response ↑ (IR > 1)

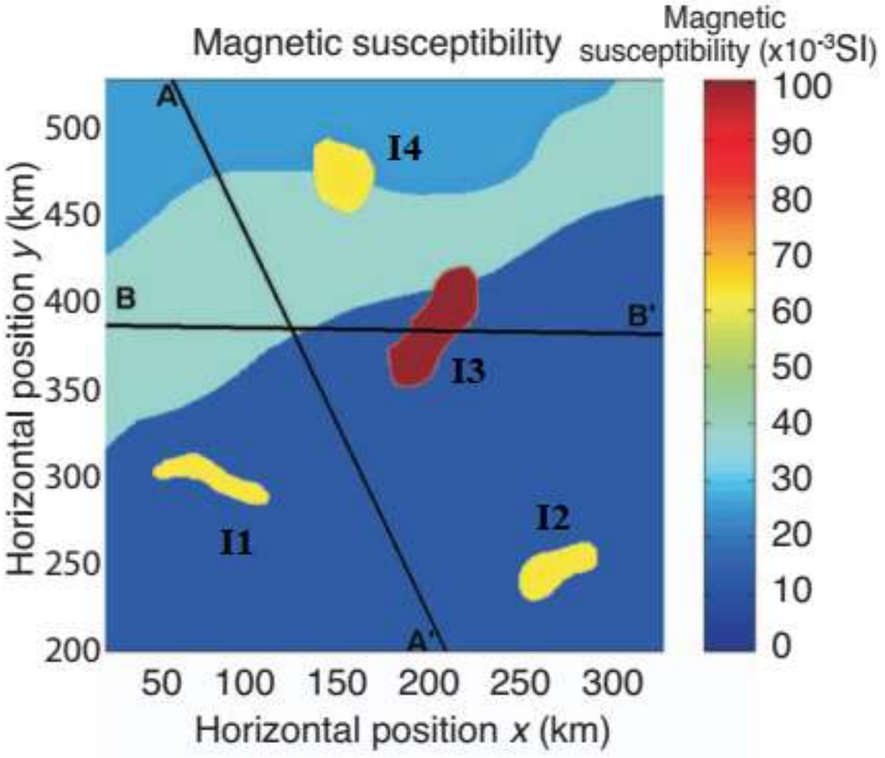

Figure 8. Magnetic susceptibility map of Bishop's model basement (Salem et al., 2008).

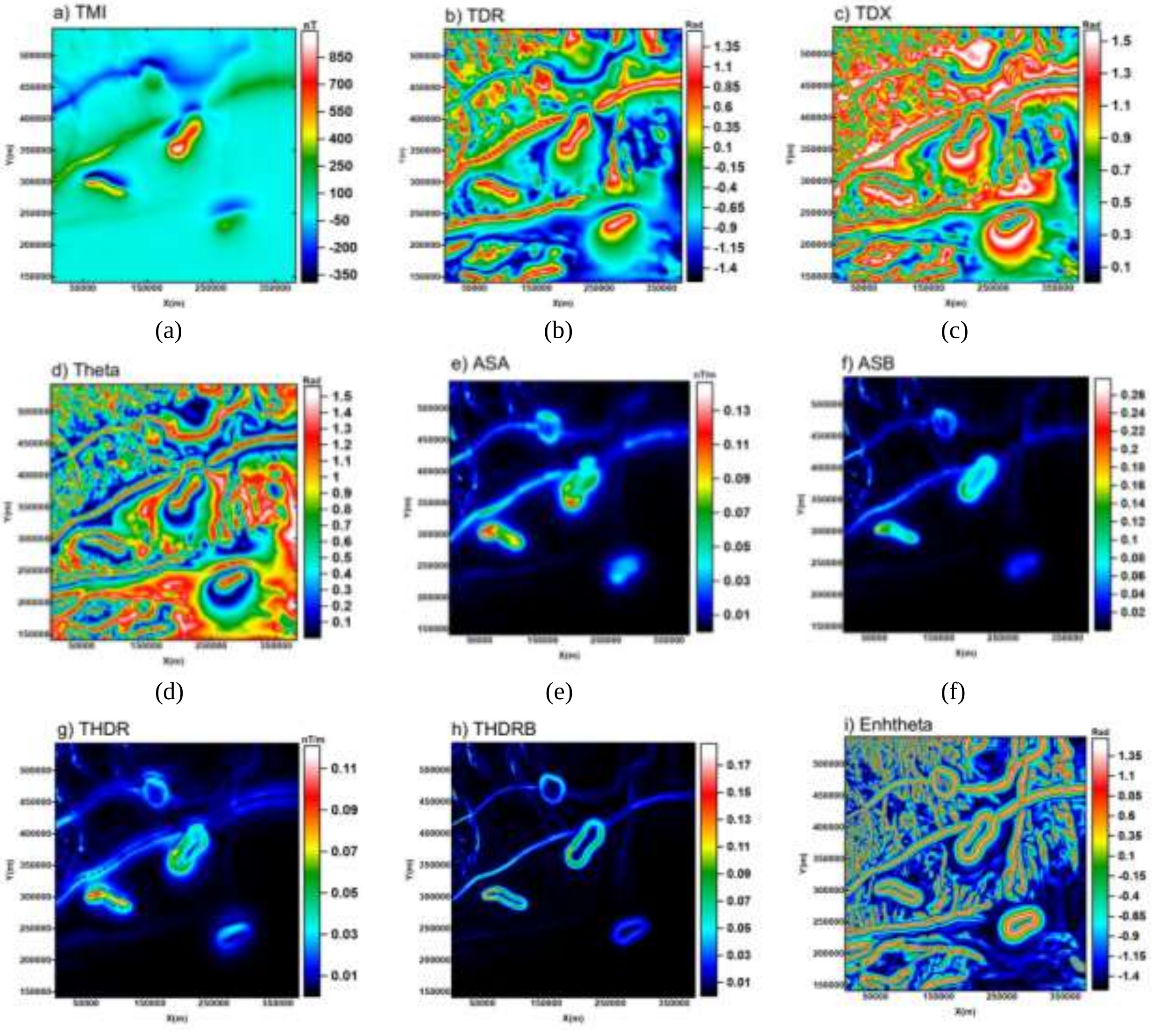

(a) (b) (c)

(d) (e) (f)

(g) (h) (i)

Figure 9. Application of different filters on magnetic data from Bishop model. a) Magnetic anomalies of the Bishop model with susceptibility variation shown in Figure 8. b) TDR map of the data in a. c) TDX map of the data in a. d) Theta map of the data in a. e) ASA of the data in a. f) ASB of the data in a. g) THDR map of the data in a. h) THDRB map of the data in a. i) Enhtheta map of the data in a.

The TDR, TDX, and Theta filters of the Bishop model are shown in Figures 9b-9d, respectively. TheTDR filter detects source edges diffusely and the detected edges are broader than actual size. The Theta and TDX maps contain more detail and better accuracy than the tilt angle (TDR), however, their sensitivity diminishes with increasing source depth. The edges estimated by TDX and Theta filters are still larger than those used in reality and create a widespread pattern.

Figures 9e and 9f show the ASA and ASB filters, respectively. Both filters produce similar results for shallow and deep anomalies; however, the ASB filter is able to normalize the anomalies and discriminate them with higher quality (less diffuse effect).

Figure 9g and 9h show the THDR and THDRB filters, respectively. These filters reveal source edges with high accuracy and sharpness, performing much better in edge detection than ASA and ASB. However, they still provide limited information for deep structures.

Finally, Figure 9i shows the Enhtheta filter applied to the magnetic dataset in 9a, (computed for k=0.15 and k is optimized using sensitivity analysis described previously). The maximum value of this filter represents the anomaly edges. This filter allows more accurate edge estimation for both shallow and deep sources (with a greater sharpness), simultaneously, compared to other filtering approaches. As seen in the image, the intrusion boundaries are defined as closed continuous lines. This filter is able to normalize the map and resolves all edges (linear or circular features), including those that other methods failed to resolve.

5. Real example

Figure 10a shows an aeromagnetic dataset from the Bushveld Igneous Complex, South Africa. In this complex there are many economic mines, and the aeromagnetic survey was carried out for reconnaissance of such a dikes that across the region since these dikes can affect the mining operations process. The data are dominated by large-amplitude anomalies from the dikes that trend E-W and NE-SW, some of which outcrop. The field inclination and declination in the area are −50° and −20°, respectively.

Figures 10b-10d show the TDR, TDX, and Theta maps. All images are dominated by high-amplitude anomalies from the E-W dikes across the data. Figures 10e and 10f show the ASA and ASB maps, respectively. Similar to previous filters (TDR, TDX, and Theta) in these images, only the high-amplitude anomalies (E-W and NE-SW dikes) are enhanced in these images, no balancing effect is evident.

Figures 10g and 10h showed the THDR and THDRB maps of the magnetic data, respectively. In the THDR and AS images, only the high-amplitude anomalies from strongly magnetized dikes are enhanced. In contrast, the THDRB map reveals more detail than the ASB map.

The result of the proposed filter, Enhtheta (computed with k=0.12), is shown in Figure 10i. This filter and its derivative (D_x Enhtheta in Figure 10j) detect edges with high accuracy and sharpness. The method balances strong and weak anomalies in proximity and at different depths, enabling the delineation of more subtle features in the area. Moreover, lineaments associated with smaller or weakly magnetized dikes are detected with greater connectivity and sharpness. In other hands, there are several anomalies that are not distinguished by any other filters which are now clearly detected.

The lineaments interpreted from the Enhtheta filter over the Bushveld Igneous Complex correspond well with known structural and lithological boundaries. As shown in Figure 11, several major features align with mapped faults such as the Steelpoort and Zondereinde faults, while others coincide with contacts between the Marginal, Critical, and Main Zones. Additional narrow features may represent dolerite dykes or feeder conduits (Basson, 2019). Importantly, a number of newly detected lineaments do not appear on published geological maps, suggesting possible unmapped faults or internal contacts within the complex. These interpretations highlight the value of Enhtheta in enhancing structural features; however, the geological significance of the newly detected lineaments requires validation with independent field and map data.

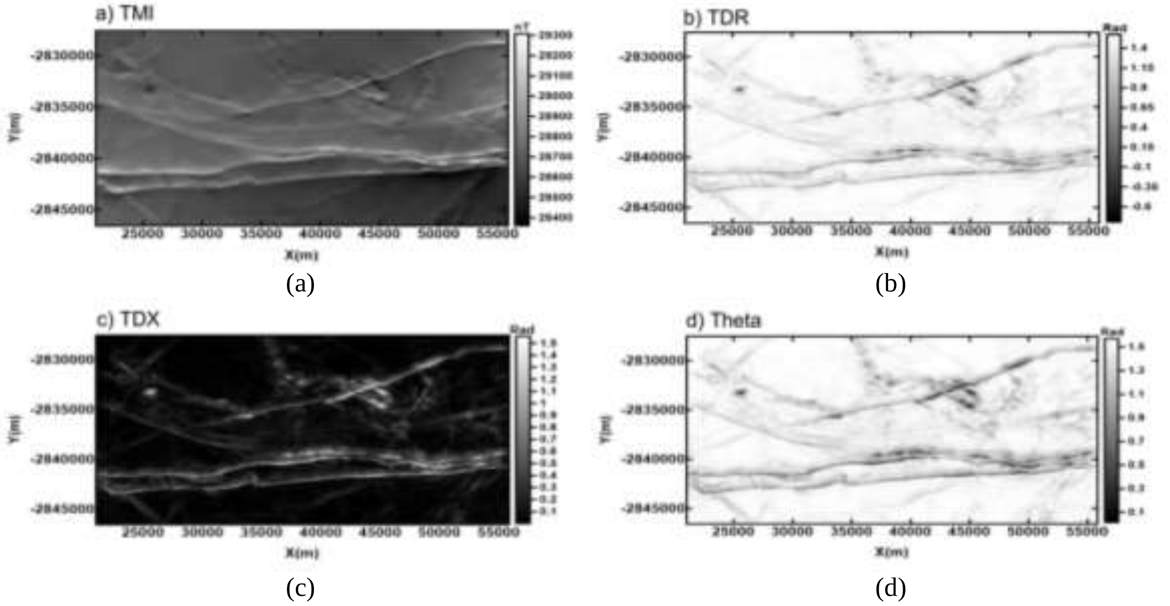

(a) (b)

(c) (d)

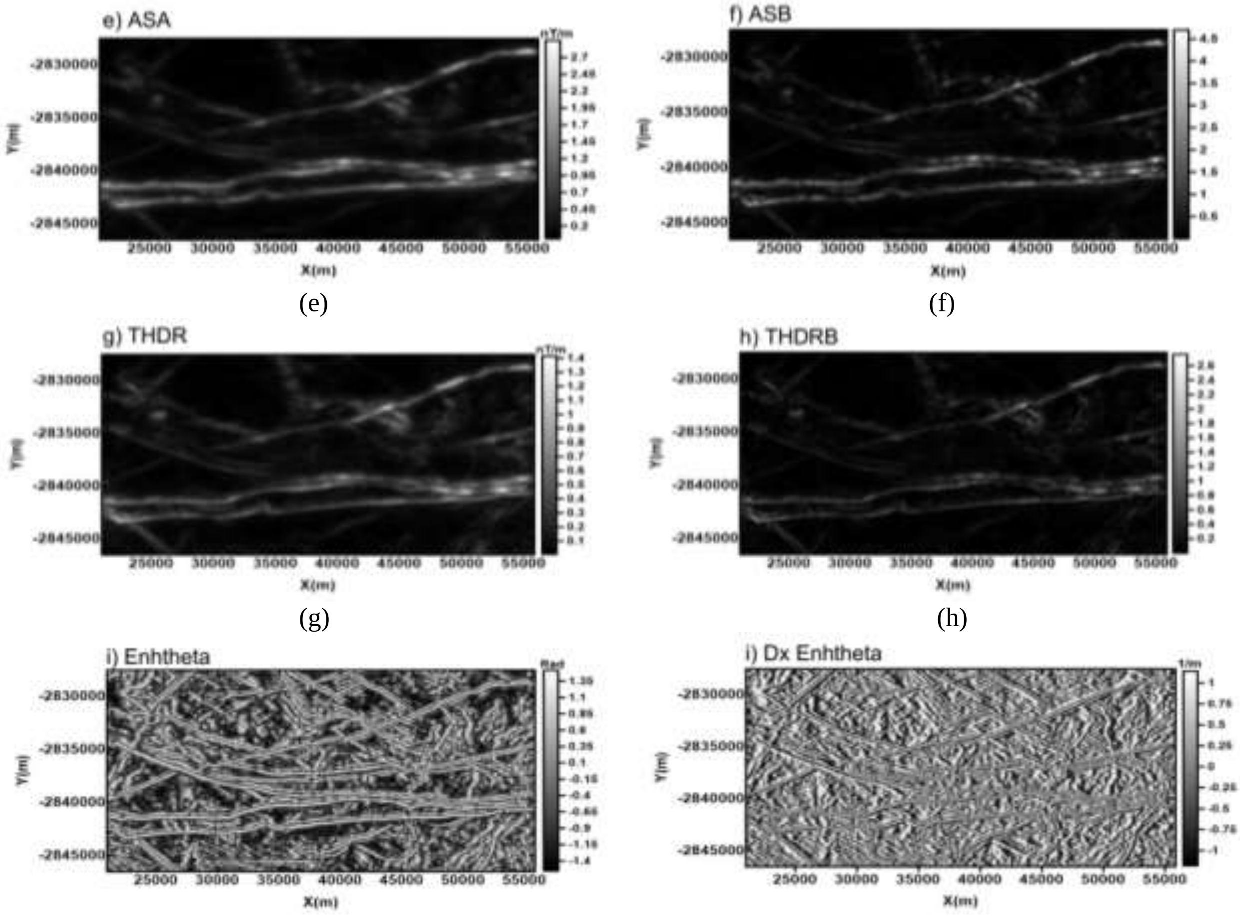

(e) (f) (g) (h) (i) (j)

Figure 10. Application of different filters on aeromagnetic data from a portion of the Bushveld Igneous Complex, South Africa. a) Magnetic anomalies of the studied area. b) TDR map of the data in a. c) TDX map of the data in a. d) Theta map of the data in a. e) ASA of the data in a. f) ASB of the data in a. g) THDR map of the data in a. h) THDRB map of the data in a. i) Enhtheta map of the data in a. j) D_x Enhtheta of the data in a.

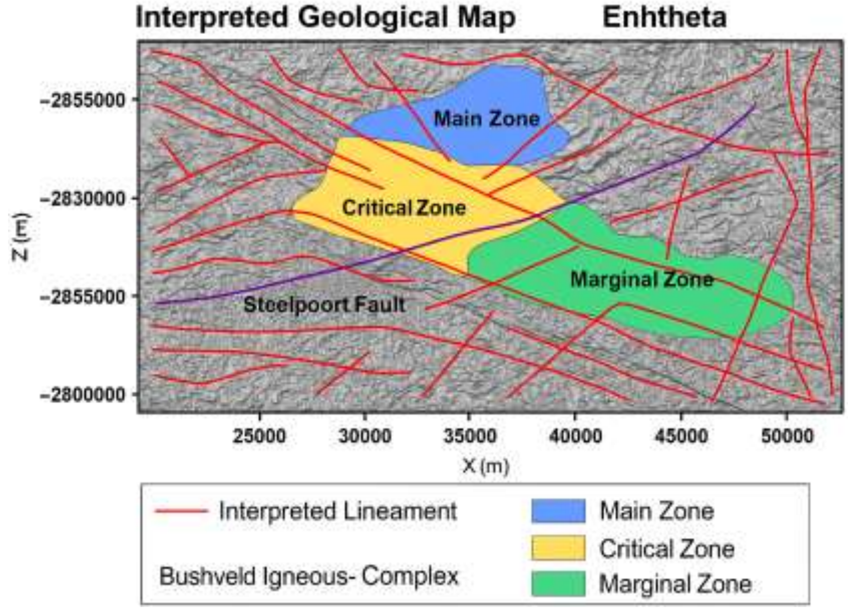

Figure 11. Geological interpretation of the Bushveld Igneous Complex based on the Enhtheta filter. The background represents the Enhtheta response, with red lines indicating interpreted structural lineaments. Major geological zones are shown in color: Marginal Zone (green), Critical Zone (yellow), and Main Zone (blue). The Steelpoort Fault is highlighted in purple. Newly identified lineaments may correspond to unmapped faults or lithological contacts and require further validation against published geological maps and field observations.

6. Limitations of the Balanced Theta Method

Although the balanced theta method has demonstrated considerable potential for delineating the boundaries of potential field data, several limitations should be acknowledged.

First, the method is sensitive to noise in the input data. Small-scale fluctuations or measurement errors can significantly affect the stability of the estimated boundaries, leading to spurious or distorted results. Therefore, careful preprocessing and noise reduction, such as upward continuation or high-pass filtering, are essential prior to its application.

Second, the performance of the balanced theta method is strongly dependent on the magnetization direction of the source body. Variations in the inclination or declination of magnetization can introduce biases in the detected boundaries, which may reduce its reliability in regions with complex or poorly constrained magnetization vectors. In such cases, using an RTP filter is suggested.

Third, the method exhibits a geometric dependence on the shape and orientation of the anomalous body. In particular, irregular or heterogeneous geometries can lead to inaccurate boundary estimations, since the underlying assumptions of the method are better suited for simpler, more homogeneous sources.

Finally, the method may suffer from non-uniqueness when applied to complex geological settings. Different subsurface configurations can produce similar boundary responses, which complicates the geological interpretation without additional constraints or supporting data.

Taken together, these limitations suggest that while the balanced theta method is a valuable tool for boundary estimation, its results should be interpreted with caution and preferably in conjunction with other geophysical techniques.

7. Conclusion

This study introduced the Enhanced Theta (Enhtheta) filter as a modification of the conventional theta method for edge detection in potential field data. The results obtained from synthetic and real datasets demonstrate that Enhtheta provides sharper and more reliable delineation of source boundaries compared to existing filters. Its principle advantage lies in balancing weak and strong anomalies, as well as shallow and deep sources, thereby reducing the diffuse edge problem inherent in the conventional theta map.

Despite these benefits, Enhtheta remains relatively sensitive to high-frequency noise and may require upward continuation for stable performance in noisy environments. Moreover, its accuracy can be affected by the magnetization direction and geometry of the causative body. Nevertheless, by enhancing boundary sharpness and improving resolution, Enhtheta offers a practical tool for simplifying and strengthening both qualitative and quantitative interpretations of potential field data.

Acknowledgment

The author thanks the Council for Geoscience (CGS), South Africa, for permission to use the aeromagnetic data from Bushveld Complex, South Africa, and also thanks Alan Reid, Richard J. Blakely, Missac Nabighian, Jeffrey D. Phillips, and Richard Smith for their constructive comments.

References

Arısoy, M.O., & Dikmen, U. (2015). Edge enhancement of magnetic data using fractional-order-derivative filters. *Geophysics*, 80(1), J7–J17.

Ansari, A.H., & Alamdar, K. (2011). A new edge detection method based on the analytic signal of tilt angle (ASTA) for magnetic and gravity anomalies. *Iranian Journal of Science and Technology, Transactions A: Science*, 35(2), 81–88.

Blakely, R.J., & Simpson, R.W. (1986). Approximating edges of source bodies from magnetic or gravity anomalies. *Geophysics*, 51, 1494–1498.

Basson, I.J. (2019). Cumulative deformation and original geometry of the Bushveld Complex. *Tectonophysics*, 750, 203–220.

Cordell, L., & Grauch, V. J. S. (1985). Limitations of determining density or magnetic boundaries from the horizontal gradient of gravity or pseudogravity data. *Geophysics*, 52(1), 118-121.

Chen, T., & Zhang, G. (2022). NHF as an edge detector of potential field data and its application in the Yili Basin. Minerals, 12, 149.

Cooper, G.R.J., & Cowan, D.R. (2006). Enhancing potential field data using filters based on the local phase. *Computers & Geosciences*, 32, 1585–1591.

Cooper, G.R.J. (2009). Balancing images of potential-field data. *Geophysics*, 74(3), L17–L20.

Cooper, G.R. (2014). Reducing the dependence of the analytic signal amplitude of aeromagnetic data on the source vector direction. *Geophysics*, 79, J55–J60.

Evjen, H.M. (1936). The place of the vertical gradient in gravitational interpretations. *Geophysics*, 1, 127–136.

Fairhead, J.D., Salem, A., Cascone, L., Hammill, M., Masterton, S., & Samson, E. (2011). New developments of the magnetic tilt-depth method to improve structural mapping of sedimentary basins. *Geophysical Prospecting*, 59, 1072–1086.

Ferreira, F.J., de Souza, J., de Bongiolo, B.E.S.A., & de Castro, L.G. (2013). Enhancement of the total horizontal gradient of magnetic anomalies using the tilt angle. *Geophysics*, 78(3), J33–J41.

Ferreira, F.J.F., de Castro, L.G., Bongiolo, A.B.S.B., de Souza, J., & Romeiro, M.A.T. (2011). Enhancement of the total horizontal gradient of magnetic anomalies using tilt derivatives: Part II—Application to real data. *SEG Expanded Abstracts*, 887–891.

Hidalgo-Gato, M.C., & Barbosa, V.C.F. (2015). Edge detection of potential-field sources using scale-space monogenic signal. *Geophysics*, 80(5), J27–J36.

Li, L., Ma, G., & Du, X. (2012). Edge detection in potential-field data by enhanced mathematical morphology filter. *Pure and Applied Geophysics*, 170(4), 645–653.

Ma, G., Liu, C., & Li, L. (2014). Balanced horizontal derivative of potential field data to recognize the edges and estimate location parameters. *Journal of Applied Geophysics*, 108, 12–18.

Ma, G. (2013). Edge detection of potential field data using improved local phase filter. *Exploration Geophysics*, 44(1), 36–41.

Mandal, A., Mohanty, W.K., Sharma, S.P., Biswas, A., Sen, J., & Bhatt, A.K. (2015). Geophysical signatures of uranium mineralization. *Geophysical Prospecting*, 63, 713–726.

Miller, H.G., & Singh, V. (1994). Potential field tilt—a new concept for location of potential field sources. *Journal of Applied Geophysics*, 32, 213–217.

Moon, W.M., Ushah, A., Singh, V., & Bruce, B. (1988). Application of 2-D Hilbert transform in geophysical imaging. *IEEE Transactions on Geoscience and Remote Sensing*, 26, 502–510.

Nabighian, M.N. (1972). The analytical signal of 2D magnetic bodies. *Geophysics*, 37, 507–517.

Nabighian, M.N. (1984). Toward a three-dimensional automatic interpretation of potential field data. *Geophysics*, 49, 780–786.

Roest, W.R., Verhoef, J., & Pilkington, M. (1992). Magnetic interpretation using the 3-D analytic signal. *Geophysics*, 57, 116–125.

Sun, Y., Yang, W., Zeng, X., & Zhang, Z. (2016). Edge enhancement of potential field data using spectral moments. *Geophysics*, 81(1), G1–G11.

Santos, D.F., Silva, J.B.C., Barbosa, V.C.F., & Braga, L.F.S. (2012). Deep-pass aeromagnetic filter to enhance deep features. *Geophysics*, 77(3), J15–J22.

Salem, A., Williams, S., Fairhead, J.D., Flanagan, G. (2007). Tilt-depth method. *The Leading Edge*, 26(12), 1502–1505.

Salem, A., Williams, S., Fairhead, J.D., Smith, R., & Ravat, D.J. (2008). Interpretation of magnetic data using tilt-angle derivatives. *Geophysics*, 73, L1–L10.

Salem, A., Williams, S., Samson, E., Fairhead, J.D., & Ravat, D. (2010). Sedimentary basins reconnaissance using tilt-depth. *Exploration Geophysics*, 41, 198–209.

Salem, A., Masterton, S., Campbell, S., Fairhead, J.D., Dickinson, J., & Murphy, C. (2013). Interpretation of tensor gravity data using adaptive tilt angle. *Geophysical Prospecting*, 61, 1065–1076.

Verduzco, B., Fairhead, J.D., Green, C.M., & Mackenzie, C. (2004). New insights into magnetic derivatives. *The Leading Edge*, 23, 116–119.

Wijns, C., Perez, C., & Kowalczyk, P. (2005). Theta map: Edge detection in magnetic data. *Geophysics*, 70(4), L39–L43.

Wang, W., Pan, Y., & Qiu, Z. (2009). A new edge recognition method. *Applied Geophysics*, 6(3), 226–233.

Williams, S.E., Fairhead, J.D., & Flanagan, G. (2005). Comparison of grid Euler deconvolution. *Geophysics*, 70, L13–L21.

Zhou, W., Nan, Z., & Li, J. (2016). Self-constrained Euler deconvolution using potential field data. *Pure and Applied Geophysics*, 173, 2073–2085.